JOURNAL OF GEOPHYSICAL RESEARCH, VOL. 97, NO. A9, PAGES 13,865–13,876, SEPTEMBER 1, 1992

Onset Conditions for Equatorial Spread F

MICHAEL MENDILLO, JEFFREY BAUMGARDNER, XIAOQING PI, AND PETER J. SULTAN

Center for Space Physics, Boston University, Boston, Massachusetts

ROLAND TSUNODA

SRI International, Menlo Park, California

The problem of day-to-day variability in the occurrence of equatorial spread F (ESF) is addressed using multidiagnostic observations and semiempirical modeling. The observational results are derived from a two-night case study of ESF onset conditions observed at Kwajalein Atoll (Marshall Islands) using the ALTAIR incoherent scatter radar and all-sky optical imaging techniques. The major difference between nights when ESF instabilities did not occur (August 14, 1988) and did occur (August 15, 1988) in the Kwajalein sector was that the northern meridional gradient of 6300-Å airglow was reduced on the night of limited ESF activity. Modeling results suggest that this unusual airglow pattern is due to equatorward neutral winds. Previous researchers have shown that transequatorial thermospheric winds can exert a control over ESF seasonal and longitudinal occurrence patterns by inhibiting Rayleigh-Taylor instability growth rates. We present evidence to suggest that this picture can be extended to far shorter time scales, namely, that "surges" in transequatorial winds acting over characteristic times of a few hours to a day can result in a stabilizing influence upon irregularity growth rates. The seemingly capricious nature of ESF onset may thus be controlled, in part, by the inherent variability of low-latitude thermospheric winds.

1. INTRODUCTION

The day-to-day variability in the occurrence of equatorial spread F (ESF) represents a continuing enigma in equatorial aeronomy. During the past decade, significant progress has been made in modeling ESF as the result of a gravitational Rayleigh-Taylor (R-T) instability arising from a "seed perturbation" [*Zalesak et al.*, 1982]. In addition, two major studies appeared that explored the cause(s) of the confusing patterns of ESF occurrence rates as a function of season and longitude [*Maruyama and Matuura*, 1984; *Tsunoda*, 1985]. In both cases, the longitudinal variability in seasonal ESF occurrence rates was linked to important geometrical relationships between solar and thermospheric ("seasonal") patterns and tilted geomagnetic dipole ("longitude") patterns. The Maruyama and Matuura study ultimately defined the seasonal-longitude conditions when ESF was *not likely* to occur, while the Tsunoda study described the seasonal-longitude conditions when ESF was *likely* to occur. Both approaches are consistent with observed long-term morphology patterns, namely, that ESF activity is high at Atlantic longitudes during northern winter, at Pacific longitudes during northern summer, and at South American and Indian longitudes during equinox periods.

The Maruyama and Matuura study based its conclusion on the theoretical framework of ESF suppression by a transequatorial neutral wind (an effect modeled in more detail in the work by *Maruyama* [1988]). Briefly, their condition for ESF activity was that the direction of thermospheric winds in the nighttime F region be close to perpendicular to the geomagnetic meridians (i.e., minimize transequatorial meridional winds). They argued that the seasonal migration of the thermospheric pressure bulge resulted in such patterns at longitudes and seasons associated with ESF activity.

Tsunoda [1985] approached the varying seasonal-longitude problem from the viewpoint of relating theoretical R-T growth rate conditions to solar-terrestrial geometrical patterns. Specifically, he showed that ESF activity can occur when a special relationship exists between the solar terminator and local magnetic field declination: when sunset is simultaneous at the conjugate E regions, the eastward polarizaton electric field is maximally enhanced and provides optimum vertical electrodynamics for ESF generation via the gradient-drift and Rayleigh-Taylor instabilities.

Taken together, the picture that has emerged from theory and observation is as follows: (1) At a given site, "ESF season" occurs when the sunset terminator is approximately aligned with the geomagnetic flux tubes in that region, a condition typically associated with minimal thermospheric winds along the geomagnetic meridian. (2) The R-T instability can occur at such sites during the postsunset period in response to a "seed perturbation" of unknown cause.

Observationally, plasma-depleted flux tubes containing plumes of irregularities that are detected by their radar signatures are indeed seen to occur in response to "preevent" perturbations (e.g., gravity waves) in the postsunset hours [*Tsunoda and White*, 1981; *Kelley et al.*, 1981]. Later in the night, plasma depletions observed by radio and optical methods are seen to drift into a region from the west; these are considered "fossil depletions" that were initiated after sunset at more westerly longitudes in the same region of "ESF season." Structuring of the western wall of such depletions by the gradient-drift instability can, however, provide secondary bubble formation from the vicinity of fossil depletions [*Tsunoda*, 1983].

The still elusive and therefore unsatisfactory aspect of this "standard model" is that it does not conform, on the average, to long-term observations of day-to-day ESF onset rates

Paper number 92JA00647.
0148-0227/92/92JA-00647$05.00

during the postsunset hours. Observational support for the classic scenario of a large-scale wave structure leading to plasma bubble development rests primarily on a single case study at Kwajalein [*Tsunoda and White*, 1981] and a single case study at Jicamarca [*Kelley et al.*, 1981]. Clearly, other cases exist in unpublished observations but also do a great many nonclassic cases. For example,

1. There are large numbers of onset and growth events observed that are not clearly associated with a precursor or seed perturbation of the characteristic size required by simulation studies. A "suitable size" might be an isolevel N_e perturbation extending over a scale height ($\sim$ 50 km), as used in the *Zalesak et al.* [1982] and *Gaydukov et al.* [1989] simulations.

2. There are cases of observed perturbations with the required characteristics that do not initiate instabilities during the local times and seasons when growth is optimal.

Thus the current state of affairs, one that requires both an ionosphere susceptible to an instability and the presence of a seed perturbation, does not describe the phenomena fully. In this paper, we pursue a somewhat different viewpoint, namely that during ESF season at a given location, we will assume that sufficient seed perturbations are present each night that can initiate R-T stabilities. The observational fact that they do not occur each night suggests that a damping mechanism is present intermittently to suppress ESF occurrence.

We will take the thermospheric wind seasonal-longitude ESF suppression mechanism of Maruyama and Matuura and extend its applicability to far shorter time scales than envisioned in their study. Thus, following the suggestion by *Aarons* [1991] that spread *F* irregularities can be "inhibited" occasionally during geomagnetic storms by ring current associated electrodynamical motions, we will present evidence to suggest that "surges" in a meridional wind may be the suppression mechanism not fully appreciated in earlier studies of ESF day-to-day variability and, indeed, perhaps even variability on scales of hours within a given night.

2. INSTRUMENTATION

Coordinated incoherent scatter radar and all-sky optical observations were made in August 1988, using the ALTAIR facility and the portable CEDAR imaging system located on Kwajalein Atoll (9.4°N, 167.5°E) in the Republic of the Marshall Islands. Use of ALTAIR to study ESF effects has been described in a series of papers (see, for example, *Tsunoda* [1981, 1983], and *Tsunoda et al.* [1979]). Briefly, incoherent scatter (IS) observations are made in power-only mode yielding electron densities under the assumption of $T_e/T_i = 1$ for nighttime conditions. Calibration of the IS power returns to absolute N_e (el/cm^3) is made using a nearby ionosonde, resulting in uncertainties in densities of approximately $\pm$ 10%. When the radar is directed perpendicular to the geomagnetic field, incoherent scatter returns continue to yield $N_e(h)$ profiles *unless* ionospheric irregularities of scale size $\sim$ 0.3 m ($\frac{1}{2}\lambda$ of the 422-MHz UHF transmitter signal) occur along the line of sight. Under such $\perp$B conditions, a very strong coherent backscatter occurs (typically 30-40 dB over IS levels), signalling the presence of ESF structures.

Monochromatic imaging of the large-scale *F* region plasma depletions that contain ESF irregularities typically appear as regions of low 6300-Å emission ("airglow depletions") due to the cessation of *F* region recombination chemistry in the low density ESF plumes [*Weber et al.*, 1978; *Mendillo and Baumgardner*, 1982]. At locations near the geomagnetic equator (ALTAIR is at 4.3°N magnetic dip latitude), the postsunset rise of the *F* region results in very low ambient 6300-Å levels. Under such conditions, airglow depletions are best imaged in the faint 7774-Å emission from direct O^+/e^- recombinations that depend more on the total electron content (TEC) of the $N_e(h)$ profile and not its altitude of peak density [*Mendillo et al.*, 1985]. The focus of this paper is not on imaging airglow depletions per se but rather on ambient 6300-Å airglow patterns just prior to typical onset times, a period when 6300-Å emission is particularly sensitive to vertical motions.

The basic design of the CEDAR all-sky imaging system used in conjunction with ALTAIR in August 1988 is described by *Baumgardner and Karandanis* [1984]. Figure 1 illlustrates the field of view (FOV) of the all-sky imager, together with the locations of the geomagnetic equator, the direction of the ALTAIR east-west $\perp$B scan that senses ESF irregularities, and several geometrical features related to local solar and geomagnetic conditions. As shown in this figure, the ALTAIR east-west scans and the imager's FOV span $\pm$ 30 min of local time. Throughout this paper we will quote solar local time at ALTAIR using the relationship LT = UT

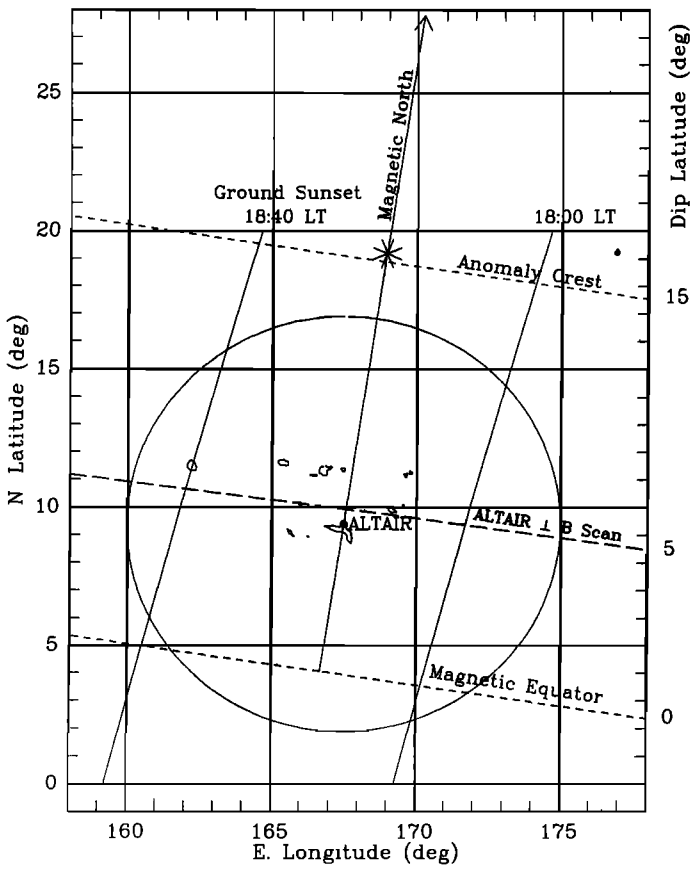

Fig. 1. Map of the Kwajalein Atoll, Marshall Islands, sector showing the field of view for a 150° imaging system evaluated for a 6300-Å emission height of 300 km. The geomagnetic equator, the typical location of the northern crest of the equatorial anomaly at 15° N geomagnetic, and the ALTAIR $\perp$B scan locations are given. A geomagnetic meridian is shown at declination 8.5°; the asterisk indicates the point in the *E* region at 110 km that maps to 600 km above the geomagnetic equator. The ground sunset terminator is shown for 1800 and 1840 LT on August 14, 1988.

+ 1110 appropriate for 167.5°E. The exact local times of features to the east or west of this meridion are not of crucial importance to the results that follow. Finally, we note that ground sunset (defined as zenith angle to the center of the solar disk $\chi_s = 90°\ 50'$) in mid-August occurs at 0707 UT (or 1817 LT) and that low light level imaging observations can begin about 1 hour later.

3. OBSERVATIONS

3.1. *Radio Diagnostics*

On the nights of August 14 and 15, 1988, ALTAIR observations were made from 0700-1000 UT in order to examine the postsunset conditions associated with onset of F region instabilities. Plate 1 portrays a series of the ALTAIR $\perp$B scans for the case study nights. On August 14, during the postsunset transition period ($\sim$ 1800 - 2000 LT), a single plume was observed near 1907 LT at very large ranges ($\sim$ 800 km) to the east of Kwajalein. However, this early plume did not signify a night of high irregularity activity for the Kwajalein sector ionosphere. As shown in Plate 1*a*, the ALTAIR radar showed no additional plume activity over the entire transition period on August 14; only some minor bottomside backscatter occurred at similar eastern longitudes $1\frac{1}{2}$ hours later. In Plate 1*b*, on August 15 near 1940 LT, a dramatic ESF backscatter plume developed above ALTAIR during the $\sim$ 35 min period between successive scans. As shown in Plate 1*b*, observations continued to 2336 LT and showed the continuation of ESF plume activity throughout the region sampled. Note that the large plume at 1940 LT in Plate 1*b* had no obvious large-scale seed perturbations as envisioned from the simulation work of *Zalesak et al.* [1982]. It is the common nature of such events that prompts us to assume that other factors must be acting to inhibit essentially omnipresent, difficult to detect, seed perturbations from developing into ESF plumes.

In trying to understand why August 15 is an unstable ("normal") night and August 14 the stable (or "abnormal") night, we first look at local ionospheric conditions. In Figure 2 we present the electron density profiles extracted from the near-zenith portions of the $\perp$B scans taken on both nights. There are differences between August 14 and 15 but not major ones. For example, at 1904 LT on August 15, the scan prior to plume development has $h_{max} \sim 475$ km, a value similar to the h_{max} at a comparable time (1858 LT) on August 14.

Vertical plasma drift patterns can be inferred from the profiles in Figure 2. Displacements of the 10^5el/cm^3 levels, averaged over the 1800-1900 LT period, yield vertical drifts of 46 m/s on August 14 and 48 m/s on August 15 (Figure 3*a*). Figures 3*b* and 3*c* help place the ALTAIR derived vertical motions in context with earlier local time motions observed by a KEL ionosonde operating on Kwajalein during August 1988. The virtual heights of the F layer's lowest point of reflection ($h'F$) are shown at 10 min intervals. These data are plotted in Figure 3*b* for August 14

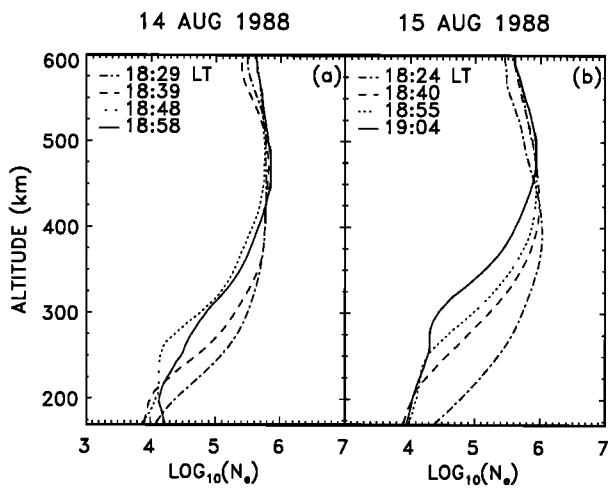

Fig. 2. Vertical electron density profiles extracted from ALTAIR scans shown in Plate 1. (*a*) August 14, 1988 and (*b*) August 15, 1988. The individual profiles are used in estimates of instability growth rate parameters during the 1800-1900 LT period when instability onset conditions are likely to occur.

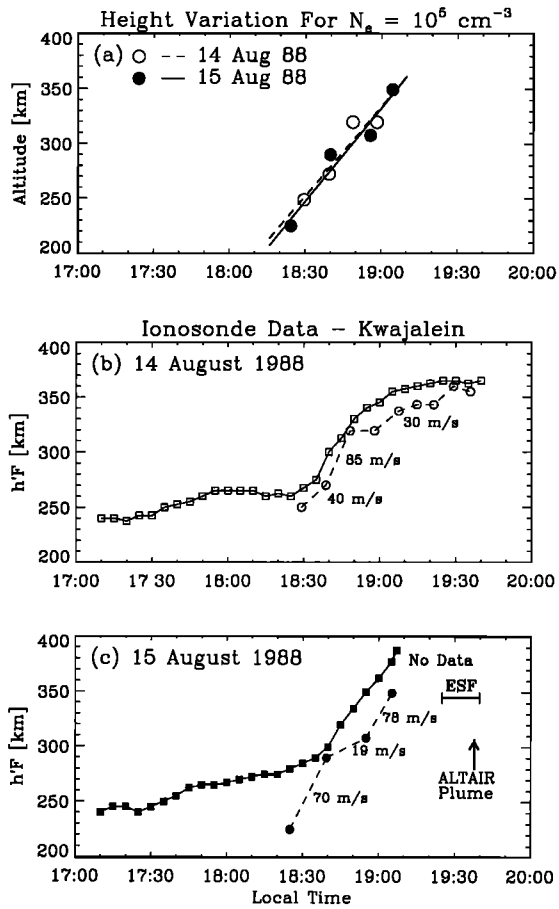

Fig. 3. (*a*) Time evolution of the $N_e = 10^5$ el/cm^3 levels from the profiles given in Figure 2. The best fit straight lines give vertical plasma drift estimates of 45.6 m/s on August 14 and 47.5 m/sec on August 15. (*b*) Observations (open squares) of $h'F$ (the lowest virtual height of F region echoes) made on Kwajalein using an Australian-made KEL ionosonde on the night of August 14, 1988. ALTAIR observations of the 10^5el/cm^3 contour level are shown for comparison (open circles). The effective drifts derived from successive points are indicated; the peak drift at 1834 LT is nearly twice the best fit value of 46 m/s taken over the full LT period shown in Figure 3*a*. (*c*) Same as Figure 3*b*, but for August 15, 1988. A no-data segment and the times of spread F effects are indicated. Note that the ionosonde sensed ESF onset approximately 15 min before the scanning ALTAIR radar passed the plume. This further reduces the plume development time discussed in the context of ALTAIR-only observations in Plate 1*b*.

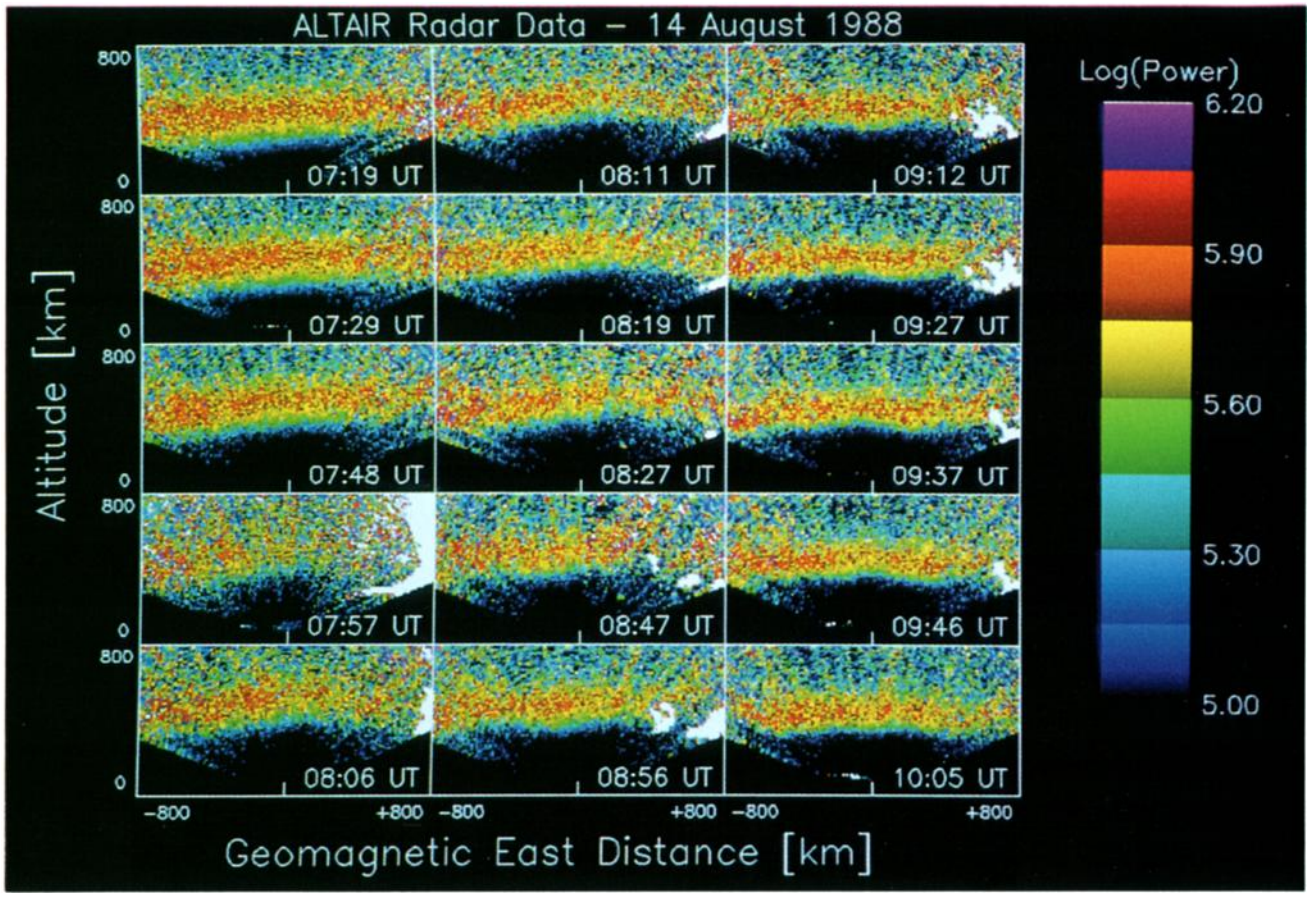

Plate. 1*a*. ALTAIR scans along the ⊥B direction shown in Figure 1 at selected times during the postsunset transition period (0700 - 0830 UT, corresponding to 1810 - 1940 LT) for August 14, 1988. Saturated radar echoes from ESF backscatter appear white. Note that the single scan at 0757 UT (1907 LT) was made using VHF, while all other scans were made using ALTAIR's UHF frequency. This results in a larger apparent plume size for the lower-frequency scan.

and Figure 3*c* for August 15, together with point-to-point ALTAIR 10^5el/cm^3 contour rise rates. After ~ 1830 LT, and for heights above 250 km, there is evidently good agreement between inferring vertical drifts by either the $h'F$ or 10^5 N_e contour rise method. While changes in electron densities below h_{max} can result from recombination loss, the validity of this technique has been demonstrated in some detail by *Tsunoda and White* [1981] and *Bittencourt and Abdu* [1981]. The more important feature in Figure 3 is the relatively sudden onset of vertical motions near ~ 1840 LT. This time is associated with the passage of the sunset terminator past the local magnetic meridian — the condition for releasing successive flux tubes from E region to F region control [*Tsunoda*, 1985]. Note, however, that the release of the F region occurs prior to actual sunset in the E region. At Kwajalein, 1840 LT corresponds to a solar zenith angle of χ_s ~ 96°, rather than to sunset at ~ 110 km (where χ_s ~ 101° at 0750 UT or 1900 LT). *Trost* [1979] has shown that E region densities near sunset are typically in a rapid transition through the 10^4 el/cm^3 value when χ_s reaches ~ 95°.

3.2. *Optical Diagnostics*

Airglow observations provide a single parameter (column emission) that can be used to infer ionosphere/thermosphere conditions. For 6300-Å emission, strong signals imply substantial ionospheric loss and therefore a relatively low F region. Obviously, an IS radar can measure this directly; the utility of all-sky imaging is that it records line-of-sight emission simultaneously over ~ 3 million square kilometers (the 15° diameter latitude-longitude circle shown in Figure 1). Thus a single image sets the context for more detailed line-of-sight radar scans across the region of interest.

In Plate 2, 6300-Å images are presented for the postsunset periods sampled by ALTAIR in Plate 1. In the top set of images (August 14), the brightness to the left (west) in the first image represents emission from regions closer to sunset. The subsequent images show weak airglow levels (~ 25R) throughout the field of view. In the bottom set of images (August 15), the same sunset glow followed by low 6300-Å levels is observed, except for the brightness to the north (top) of the field of view. Note that at the locations of the ALTAIR ⊥B scan direction given in Figure 1 (essentially the left to right diameter of the image), the optical signatures are virtually identical on each night, thus conforming to the similar radar observations in Plate 1 and Figure 2 prior to ESF onset on August 15. The unique contribution of the imaging data is to point out that while similar observations resulted from the E-W radar scans made on August 14 and 15, there was a marked difference in ionospheric structure north-to-south that was not sampled by the radar.

4. DISCUSSION

4.1. *Estimates of Instability Growth Rates*

The ALTAIR data portrayed in Figure 2 can be used to examine instability growth rates. As shown by *Zalesak and*

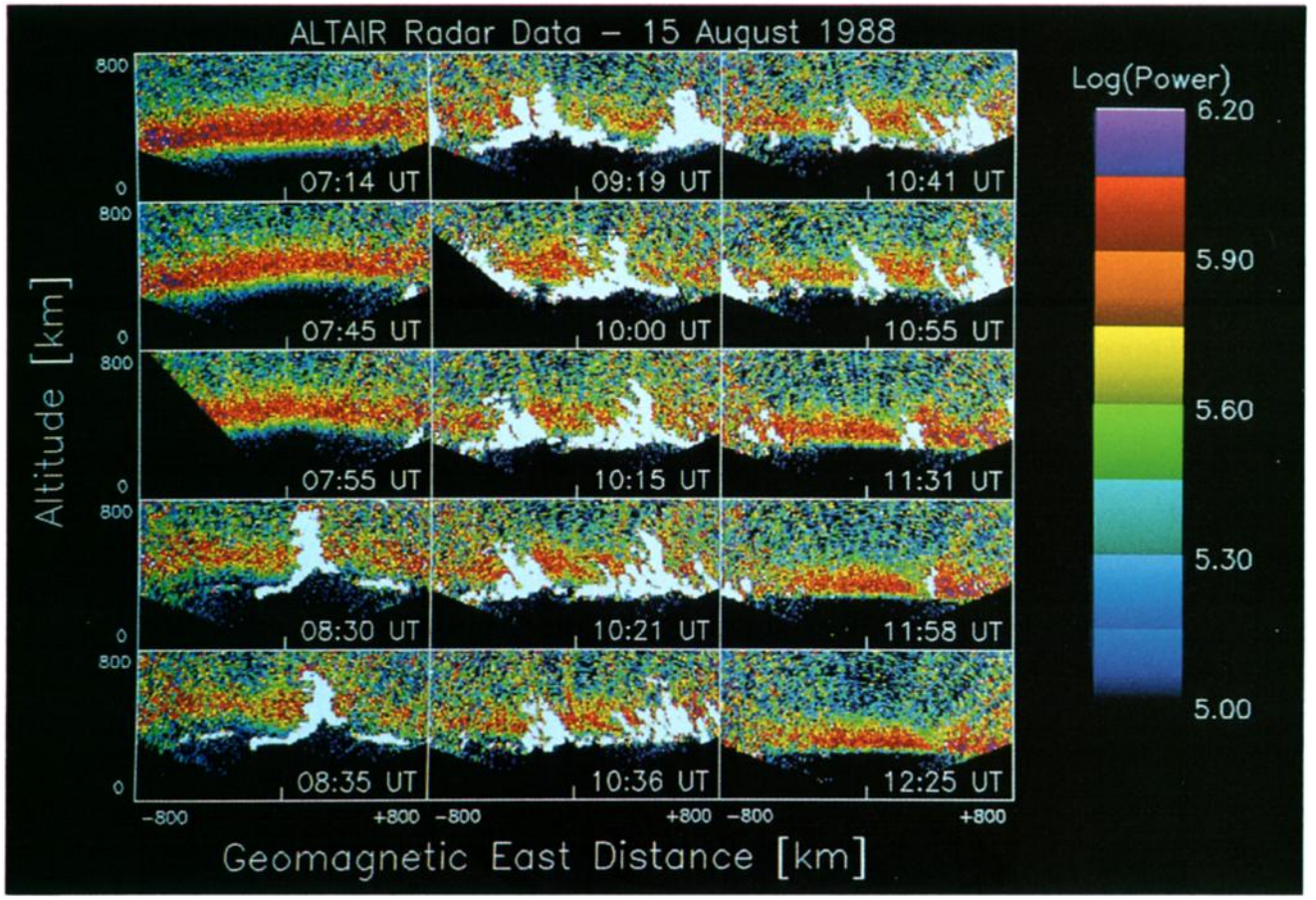

Plate. 1*b*. Same as Plate 1*a* except for August 15, 1988.

Ossakow [1982], the full growth rate for the R-T instability is given by

$$\gamma = \left[\mathbf{V}_p - \mathbf{U}_n - \frac{\mathbf{g}}{\nu_{in}}\right] \bullet \frac{\sum_p^F}{\sum_p^{E,S} + \sum_p^F + \sum_p^{E,N}} \quad \frac{\nabla N_T}{N_T} - R_T \tag{1}$$

The term in brackets gives drifts due to electric fields, neutral winds and gravity; the middle terms are Pedersen conductivities and flux tube contents (defined below), and R_T is the plasma recombination rate. Each of these terms is a geomagnetic flux-tube-integrated quantity extending from the E region in one hemisphere, including the full transequatorial F region, to the E region in the other hemisphere. The coordinate system is positive for upward, northward, and eastward. In evaluating each of the terms in (1), we are guided by the concepts described by *Haerendel et al.* [1992]. Specifically, the flux-tube-integrated electron density (N_T) is given by the total electron content of the flux tube:

$$N_T = \int N_e(s) \quad A(s)ds \tag{2}$$

where $A(s)$ is the flux tube cross-sectional area at the element of arc ds along the field line, normalized by unit area at the magnetic equator, and the integration is conducted along the entire field line. The gradient of N_T is then reduced to one dimension perpendicular to the flux tubes and can be evaluated as height above the geomagnetic equator as

$$\frac{\nabla N_T}{N_T} = \frac{1}{N_T} \quad \frac{dN_T}{dh} \tag{3}$$

The flux-tube-integrated Pedersen conductivities for each ionospheric region are

$$\sum_p = \int \frac{N_e M_i \nu_{in}^{local}}{B^2} Ads \tag{4}$$

where M_i is ionic mass, ν_{in}^{local} the local ion-neutral collision frequency, and B the local geomagnetic field strength [see *Kelley*, 1989].

The integration along the entire flux tube in (4) is divided into three segments, with $\sum_p^{E,S}$ as the contribution from the E region at the southern end of the flux tube; $\sum_p^{E,N}$ as the contribution from the E region at the northern end of the flux tube; and $\sum_p^F$ as the contribution from the full F region spanning the magnetic equator.

The remaining terms in (1) must be integrated taking into account the local electron densities throughout the flux tubes. Thus for the dynamical terms $\mathbf{V}_p$, $\mathbf{U}_n$, and $\mathbf{g}/\nu_{in}$, the vector product with $\nabla N_T/N_T$ isolates the $\perp B$ components. For plasma drift,

$$\mathbf{V}_p = \frac{1}{N_T} \int v_p N_e \quad Ads \tag{5}$$

where v_p is $\perp B$ ($\mathbf{E} \times \mathbf{B}$ drift) and represents the drift of the flux tube.

For the neutral wind effect, the component $\perp B$ is the important term and thus

$$\mathbf{U}_n = \frac{1}{N_T} \int U_m sin\ I \quad N_e \ Ads \tag{6}$$

where U_m is the meridional component of the total wind vector and I is the magnetic inclination angle.

Similarly, for the gravitational/collisional term,

$$g = \frac{1}{N_T}\int g^{local} \cos I \; N_e \; Ads \qquad (7a)$$

and

$$\nu_{in} = \frac{1}{N_T}\int \nu_{in}^{local} N_e \; Ads \qquad (7b)$$

The chemical recombination rate term R_T again extends over the entire flux tube, with local values of R equal to αN_e in the E regions, and β in the F region, where α and β are loss coefficients, and thus

$$R_T = \frac{1}{N_T}\int R^{local} N_e \; Ads \qquad (8)$$

Equation (1) shows that if both ends of a field line pass into darkness at nearly the same time, the condition for "spread F season" at a given latitude [*Tsunoda*, 1985], the E region conductivities ($\sum_p^{E,S}, \sum_p^{E,N}$) decrease and the ratio of F region to total tube conductivities appearing in equation (1) approaches unity. Under such conditions, the use of local equatorial quantities provides a good framework in which to examine growth rate characteristics [*Hanson et al.*, 1986]. Thus, while we will return to flux-tube-integrated arguments in subsequent sections, we think it instructive to use actual observations, i.e., the ALTAIR $N_e(h)$ profiles, and evaluate local growth rates first using linear R-T theory [*Ossakow et al.*, 1979; *Ossakow*, 1981]. This also avoids the uncertainties and assumptions that must be employed in models of flux-tube-integrated quantities. Following *Ossakow* [1981], we have as the R-T growth rate

$$\gamma_o = \frac{g}{\nu_{in}} L^{-1} - \beta \qquad (9)$$

where g, ν_{in}, and β are local values, and

$$L^{-1} \equiv \frac{1}{N_e}\frac{dN_e}{dh}$$

is the inverse gradient scale length of the background $N_e(h)$ profile. To examine separately the cases of growth rates computed without (γ_o) and with (γ') the electrodynamic drift term, we rewrite equation (9) with V_p, an upward $\mathbf{E} \times \mathbf{B}$ drift, as

$$\gamma' = \gamma_o + V_p L^{-1} \qquad (10)$$

The MSIS model [*Hedin*, 1987] for the neutral atmosphere, evaluated for ALTAIR's location at 1900 LT on August 14 and 15, 1988, yielded essentially identical thermospheres on each night. The O^+ collision frequency (ν_{in}) and loss rate (β) expressions, as given by *Ossakow et al.* [1979], are:

$$\nu_{in} = 2.4 \times 10^{-11} (T)^{\frac{1}{2}} N_n \qquad \beta = k_1 n(O_2) + k_2 n(N_2)$$

with $k_1 = 2 \times 10^{-11}\ (300/T)^{0.4}$ cm^3/s and $k_2 = 8 \times 10^{-14}\ (T/300)^2$ cm^3/s, $T > 750$°K, were used with MSIS input parameters to obtain the altitude profiles given in Figure 4.

The gradient length parameter (L^{-1}) in equation (9) was evaluated for the electron density profiles in Figure 2, and the results are portrayed in Figures 5*a* and 5*d*. L^{-1} is the key spatial parameter in (9) and (10) that permits the instability to occur, while the dynamical factors g/ν_{in} and V_p that precede it govern the rate at which it occurs. Thus with the L^{-1} yielding ~ 0.04 km^{-1} on both August 14 and 15,

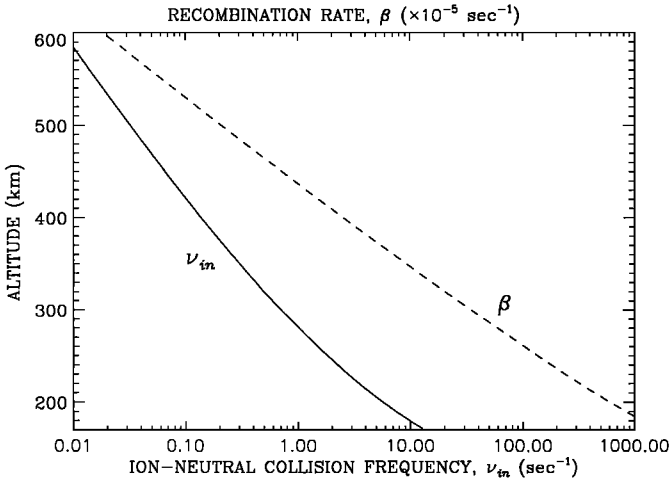

Fig. 4. Altitude dependence of two parameters used in Rayleigh-Taylor growth rate estimates. The ion-neutral collision frequency and the F region loss coefficient were evaluated using reaction rates given in the text and the MSIS neutral atmosphere model.

it would appear that both nights had bottomside gradients suitable for instability growth. As mentioned in conjunction with Figures 3 and 4, the dynamical terms were comparable on each night and thus equation (10) results in similar values (within a factor of 2) for the growth rates (γ_o and γ') on each night (see Figures 5*b*, 5*e* and 5*c*, 5*f*).

As shown in Figure 5, the L^{-1} parameter is positive over the entire bottomside region (200 km $< h <$ 500 km), and thus the negative γ' values in Figures 5*c* and 5*f* at heights below 300 km are due to the high β values there (see Figure 4). Our conclusion from these estimates is that in the absence of significant neutral wind effects, growth rates of $\gamma = 2 \times 10^{-3}$ s^{-1} near 300 km were present on both nights. The associated growth time ($\tau = \gamma^{-1}$) of 500 s ($\sim$ 8 min) is consistent with plume development in about four growth periods, as shown in Plate 1*b* for the night of August 15. The ionosonde data given in Figure 3*c* suggest that plume development may have occurred in only two growth periods.

4.2. *Airglow Morphology at Low Latitudes*

The differences in N-S airglow structure shown in Plate 2 need to be interpreted in terms of the morphology of the low-latitude ionosphere. As discussed, for example, in *Anderson et al.* [1981], the equatorial anomaly is created by electrodynamical motions that result in a low peak density F region at high altitudes near the equator, in contrast to a high-density F region at lower altitudes near $\sim \pm 15°$ magnetic latitude. These crests of the anomaly have strong 6300-Å airglow signatures that form the so-called intertropical arcs first described by *Barbier et al.* [1961]. On August 15 (lower panel of Plate 2) we have a classic manifestation of this pattern. August 15 is thus a "normal night" in terms of transequatorial structure; August 14 is "abnormal" in that no N-S gradient (associated with an intertropical arc) is visible from Kwajalein. Given that the ionospheric structure and vertical rise velocities determined by ALTAIR (Plate 1 and Figure 2) were not significantly different, the electrodynamical "fountain effect" associated with the equatorial anomaly was probably similar on both nights.

It is crucial to the argument that follows to demonstrate this point, namely, that the airglow pattern differences on August 14 and 15 do not result simply from changes in location of the equatorial anomaly. While ALTAIR did not con-

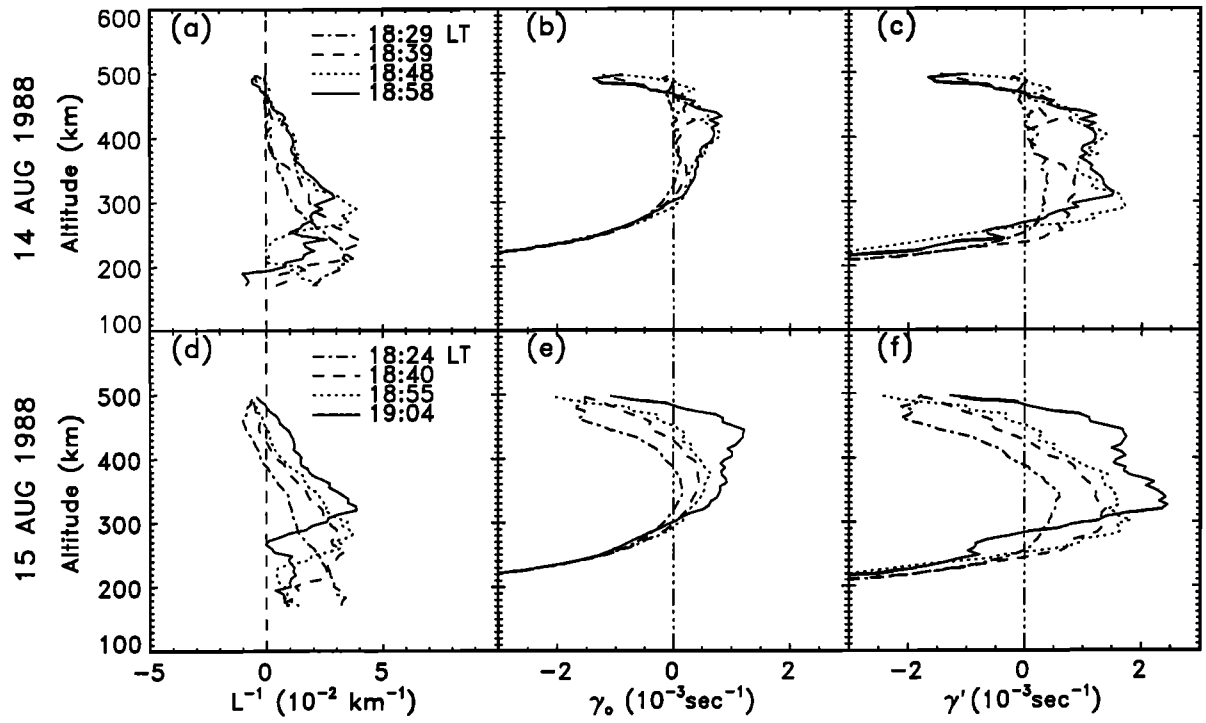

Fig. 5. Altitude dependence of the inverse scale length (L^{-1}) parameter and the R-T local growth rate for no vertical plasma drift (γ_0), and with plasma drift (γ'). The upper panels are for August 14 and the lower panels are for August 15.

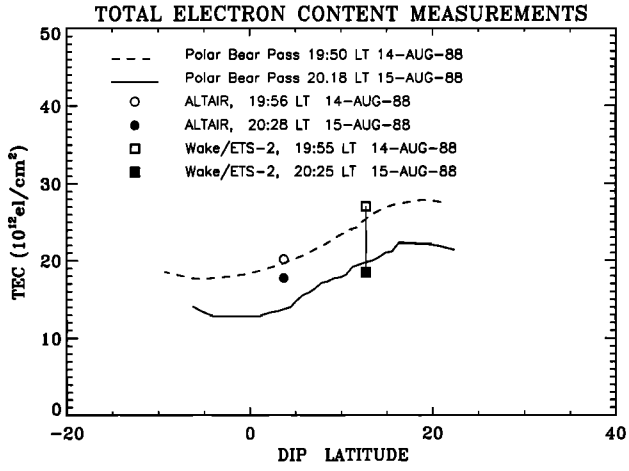

Fig. 6. Latitude structure of total electron content (TEC) obtained by three methods on the nights of August 14 and 15, 1988. The dashed and solid lines give satellite radio beacon observations of TEC made from Kwajalein using the radio beacon experiment on the Polar BEAR satellite [*Fremouw and Lansinger*, 1989]. The open and solid squares give TEC measured from Wake Island using polarimeter observations of the 136 MHz beacon on the geostationary satellite ETS-2 (R. Doe and J. Klobuchar, private communication; 1991). The open and solid circles give ALTAIR derived TEC over the height range 150-600 km, with constant scale height extrapolation from 600 to 2000 km. All data sets suggest that the structure of the Appleton anomaly region was very similar on both August 14 and 15.

duct north-south scans on August 14 and 15, satellite radio beacon (SRB) observations of the ionospheric total electron content (TEC) were made over an extensive latitude range. Figure 6 gives TEC latitudinal profiles obtained from the SRB experiment on the Polar BEAR satellite [*Fremouw and Lansinger*, 1989] obtained on the nights of August 14 and 15. These observations show that the overall structure of the anomaly region did not differ significantly on these two nights. This leaves us with thermospheric dynamics as a possible source of differentiation between the two nights.

If subjected to a transequatorial (north to south) neutral wind, *F* region plasma on the northern crest of the anomaly would experience an upward component of field-aligned motion. This would move plasma away from regions of high loss (and therefore high 6300-Å production), leaving the northern sector of the images less bright than might be expected. This is precisely what is observed on August 14 in comparison to August 15.

To summarize, the major difference noted in a two-night case study of equatorial plasma instability (ESF) onset was that the meridional gradient of 6300-Å was unusual on the night of reduced ESF activity. If the reduction in brightness of the northern intertropical arc is due to uplifting effects driven by north-to-south thermospheric winds, these transequatorial winds may well be the cause of a stabilizing influence upon R-T instability growth rates in the postsunset hours.

Before discussing how neutral winds affect R-T growth rates, we note another morphological aspect of ESF occurrence rates that might be of relevance. It has long been appreciated, but not understood, that during ESF season at a given site there is a decrease in irregularity occurrence rates during periods of high geomagnetic activity in the premidnight sector [*Koster*, 1972; *Das Gupta et al.*, 1985; *Aarons*, 1991]. Nighttime thermospheric winds typically have an enhanced equatorward component during periods of global geomagnetic storms that might extend to equatorial latitudes (see Figure 2 of *Biondi et al.* [1988]). To the extent that storm-induced winds are not symmetrical with respect to the geomagnetic equator, an interhemispheric flow pattern can occur. There may be a similarity, then, between day-to-day variability in transequatorial winds related to either minor geomagnetic activity (A_p = 21 on August 14 and A_p = 5

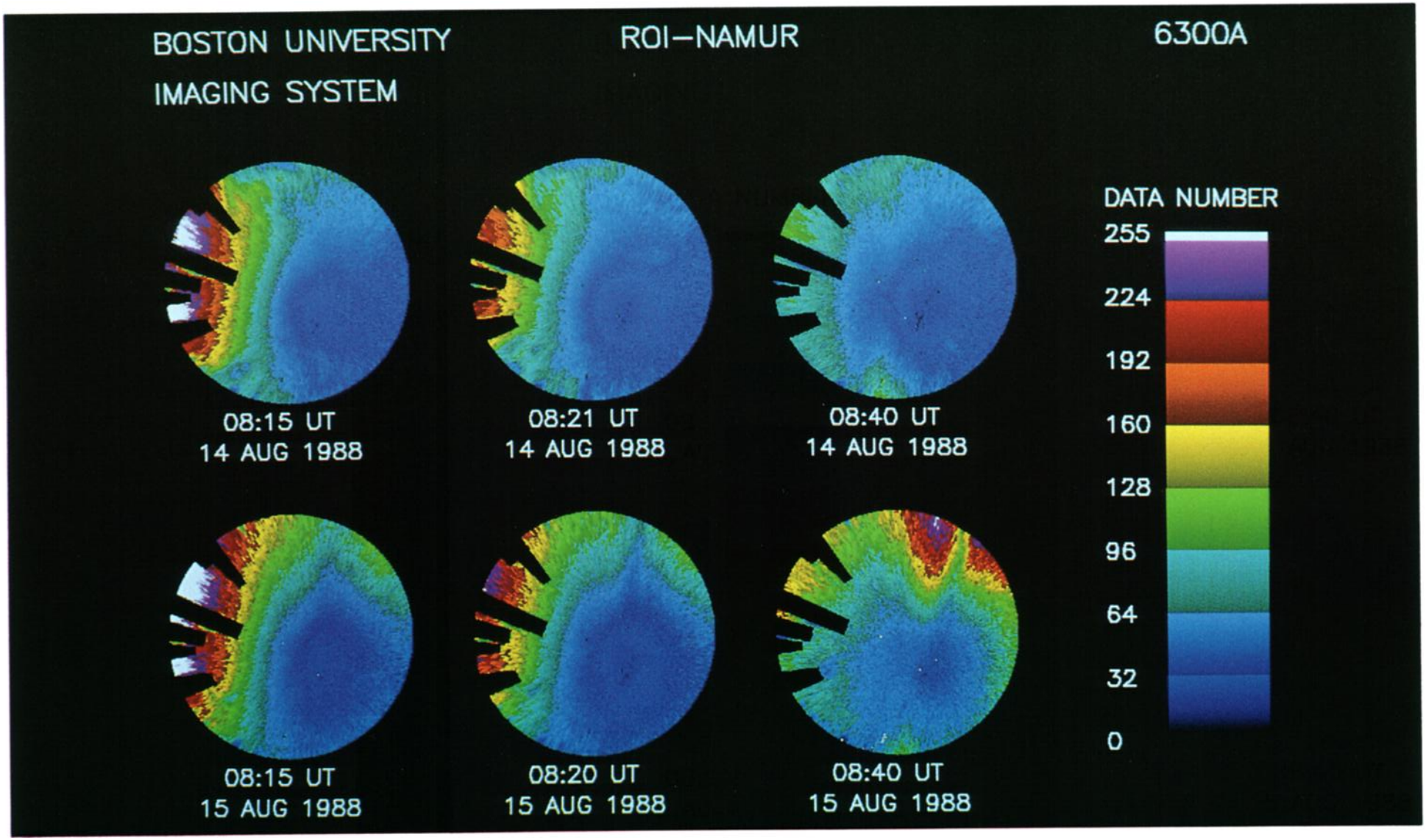

Plate. 2. A composite of 6300-Å all-sky (150° FOV) images taken at comparable times on the nights of August 14 and 15, 1988. The images have been mapped to the geographic circle shown in Figure 1, with the N, S, E, W geographic points being top, bottom, right, left. The postsunset glow seen to the west in both sets is followed by a period of uniform airglow on August 14, and a pattern of increased airglow to the north on August 15. These different latitude patterns suggest that normally present airglow morphology (August 15) was modified by an equatorward neutral wind on the night of August 14 (see text) .

on August 15) or other sources of gusts or surges (e.g., tidal coupling) and the interhemispheric winds associated with major storms, and that both inhibit the instability growth rates in the premidnight sector.

4.3. *The Effect of Neutral Winds on Instability Growth Rates*

The effect of a transequatorial neutral wind upon R-T growth rates has been addressed by *Maruyama* [1988]. Simulation results showed that large meridional winds could be associated with periods of reduced growth rates (γ). The suggested suppression mechanism involved the creation of more molecular ions (O_2^+, NO^+) on the downwind portion of the fieldline, thereby increasing the Pedersen conductivity (see equation (4)) more than the decrease in conductivity associated with the O^+ motion on the upwind portion of the flux tube. This results in an *E* region type load at one end of the flux tube, thereby lowering growth rates.

The nature of the wind effect can also be understood by referring to equation (1). The contribution of a southward meridional wind is to increase γ along that portion of a flux tube that is in the northern hemisphere, since the wind component (U_n) perpendicular to **B** is in the same direction as the g component $\perp$**B**. The opposite effect occurs along the southern portion of the flux tube. Rather than a simple cancellation, the interhemispheric motion of plasma from north to south results (via the U_m component $\parallel B$) in more plasma experiencing the stabilizing effect in the southern hemisphere than plasma experiencing the growth effect in the northern hemisphere, the end result being a net stabilizing influence upon the *entire* flux tube [*Zalesak and Huba*, 1991]. The same stabilizing effect would occur for a northward transequatorial wind. Thus it is the existence of a strong meridional wind, and not its actual direction, that modulates the occurrence of instability growth.

4.4. *Thermospheric Winds at Low-Latitudes*

As described in section 4.2, the airglow signature of a transequatorial wind would be a hemispheric asymmetry in the intertropical arcs. This effect was first discussed in detail by *Chandra et al.* [1973]. The increase in loss at the downwind end of the flux tube results in a higher abundance of the molecular ions that produce red line airglow ($O^+ + O_2 \rightarrow O_2^+ + O$, followed by $O_2^+ + e^- \rightarrow O^* + O$, and $O^* \rightarrow O + 6300$-Å). The simulations of *Maruyama* [1988] indeed show a modified, low-altitude distribution of molecular ions produced in this way for the case of northward wind (his Figures 7 and 8).

Modeling studies by *Meriwether et al.* [1985] showed that a surge in the meridional winds of 100 m/s would lead to easily observable changes in airglow morphology within 1-2 hours. To illustrate this point using the August 1988

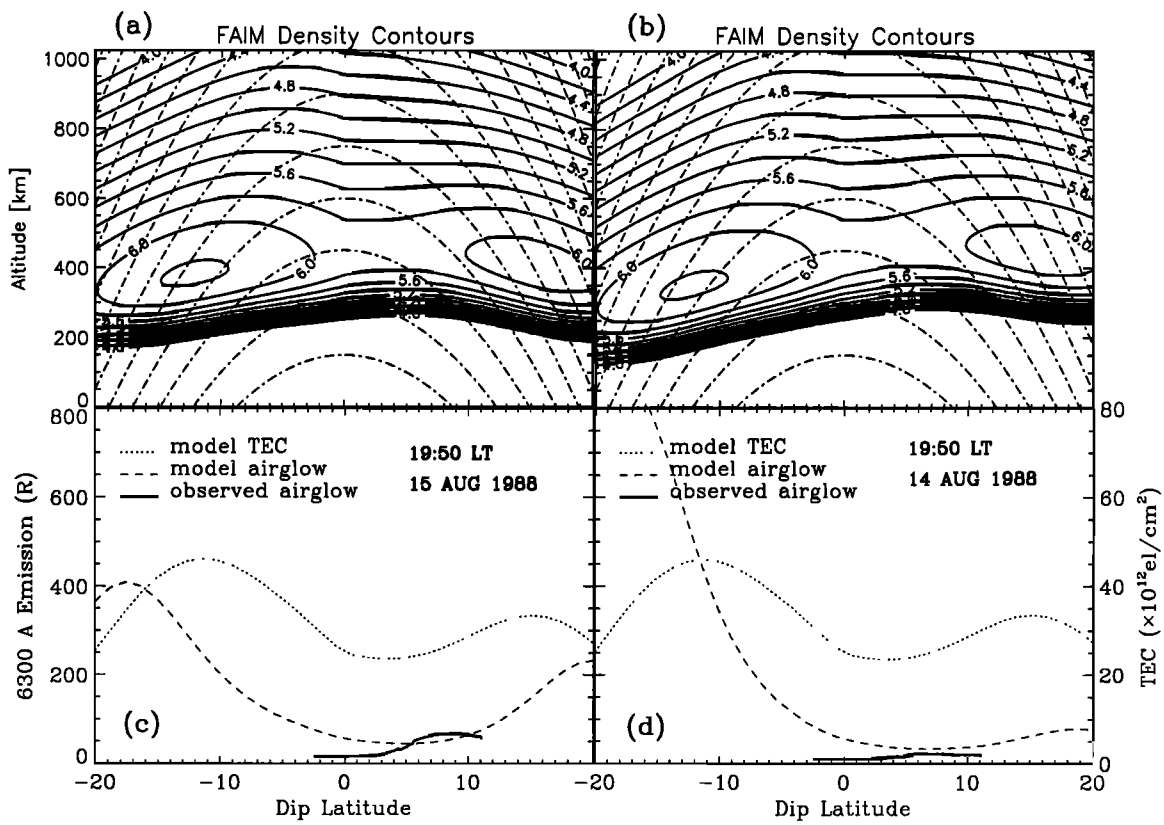

Fig. 7. (*a*) The N_e versus altitude and latitude array constructed from a run of the FAIM model of *Anderson et al.* [1989] for August 15, 1988 at 1950 LT, with the results normalized to the actual $N_e(h)$ profile measured vertically at Kwajalein on that night. The dipole field is illustrated by dashed lines. (*b*) illustrates a distorted N_e(*h*,lat) array obtained by shifting the Figure 7*a* array in a way associated with a north-south transequatorial wind (see text); (*c*) Computed and observed airglow for August 15. The airglow data were extracted from the north-south meridional diameter of the image at 0840 UT (1950 LT) in Plate 2. Absolute intensities were normalized to the model results for Kwajalein's zenith. (*d*) Computed and observed airglow for August 14. Vertically integrated TEC from the model are also portrayed in Figures 7*c* and 7*d*. The essentially identical TEC curves show that while 6300 Å is modified by vertical motions, TEC morphology is unchanged.

data sets, consider the meridional $N_e(h)$ structures given in Figure 7. The pattern in Figure 7*a* was obtained by taking the vertical $N_e(h)$ profile observed by ALTAIR at 1947 LT and filling out the (unobserved) north-south latitude-altitude structure by matching it to a run of the FAIM model of *Anderson et al.* [1989] for the same local time. The 150° field of view of an imaging system located at Kwajalein's location is indicated, and the resultant equivalent airglow pattern is portrayed. In Figure 7*b*, an asymmetry has been introduced by moving the northern crest (near 20°N) upward by 50 km, moving the southern crest downward by 50 km, while leaving the equatorial values unchanged.

The observed north-south pattern in 6300-Å intensities extracted from the images in Plate 2 at 1950 LT are shown for comparison. In Figure 7*c* we compare the "normal pattern" of airglow with actual observations made on the night of August 15; the tendency for airglow to increase to the north is evident in both curves. In Figure 7*d* we compare the "abnormal pattern" of airglow with observations made on August 14. There is a broad minimum seen in both the modeled and actual 6300-Å emission levels caused by the simulated wind effect. While these results do not represent a detailed simulation of the dynamics of transequatorial airglow patterns, they do illustrate how relatively small changes in the vertical distribution of *F* region plasma, capable of being induced by thermospheric winds, can modify the 6300-Å morphology without changing TEC structure in dramatic ways.

Rishbeth and Edwards [1989] used a "servo model" to compute the upward shift in the *F* layer's height of maximum electron density (Δh_m) associated with an equatorward wind:

$$\Delta h_m = H_i ln(\frac{W}{4H_i\beta}) \quad (11)$$

where W is the vertical component of the meridional wind = $U_m \sin(I) \cos(I)$; I is the inclination angle; H_i is the ion scale height; and β is the loss rate. Equation (11) can be used to assess the magnitude of the meridional wind required to shift the height of peak airglow emission, $h(\epsilon_{max})$, by 50 km. Using the unshifted array in Figure 7*a*, we find that near the northern crest of the Appleton Anomaly (dip lat = 15°), $h(\epsilon_{max})$ occurs at 350 km, where H_i = 70 km and $\beta = 10^{-4}$ s^{-1}. To move $h(\epsilon_{max})$ to 400 km, the vertical wind required is $W \sim 55$ m/s. For $I = 30°$, the resultant horizontal wind is $U_m \sim 130$ m/s. This represents a sizable surge in the normal meridional winds ($\sim$ 40 m/s) derived from observations and TGCM models for the Kwajalein sector [*Sipler et al.*, 1983]. Nevertheless, such effects are observed over time scales of a few hours (e.g., see Figures 2 and 4 of *Sipler et al.* [1983]).

5. SUMMARY AND CONCLUSIONS

Case studies of equatorial spread *F* (ESF) onset and growth patterns were conducted using observations from Kwajalein in August 1988. The combined use of ALTAIR incoherent scatter observations and all-sky airglow imaging demonstrated that subtle changes in north-south thermosphere/ionosphere structure were the only observational patterns capable of differentiating nights when ESF activity did and did not occur. While admittedly linked to only two nights of observations, it was shown that ESF onset occurred when the airglow patterns associated with the equatorial anomaly were essentially symmetrical about the geomagnetic equator, a condition that occurs when meridional winds are low. The ability of transequatorial neutral winds to inhibit ESF activity had been suggested by *Maruyama and Matuura* [1984] in an attempt to account for seasonal-longitude ESF occurrence rates. We suggest that the neutral wind-driven suppression mechanism should act with equivalent efficiency on a night-by-night basis, and even within a given evening.

The problem of variability in ESF activity is thus reduced to a series of conditions that are conducive to the growth of the Rayleigh-Taylor (R-T) instability:

1. In a given longitude sector, "ESF season" occurs when the sunset terminator is approximately aligned with the geomagnetic flux tubes in that region [*Tsunoda*, 1985]. Under such conditions, thermospheric winds typically have a small component along the geomagnetic meridians, and thus supression of the R-T instability is, on the average, unlikely to occur [*Maruyama and Matuura*, 1985].

2. The nightly requirements for R-T instability growth are: (1) postsunset rise of the *F* region, (2) the availability of a seed perturbation to launch the R-T mechanism, and (3) the absence of a strong transequatorial thermospheric wind.

It would appear that these latter three conditions offer sufficient flexibility to account for virtually any pattern of ESF variability at a given site. This is not a particularly pleasing way to describe a natural phenomenon. The observations presented here, when coupled to many other unpublished observations, prompt us to suggest a more specific hierarchy among the three conditions. First, the postsunset rise of the equatorial ionosphere is present on virtually every night of ESF season at a given site (see, for example, *Fejer et al.* [1989], for drift patterns at Jicamarca). Thus the lack of a rising *F* region is probably not the major source of variability in ESF occurrence. The required seed perturbation is more problematic in that observations exist of ESF development with and without precursor signatures of a seed. It is not obvious that the seeding perturbation will always be above the threshold of detectability of the instrument that senses the ESF activity. Thus our tendency is to treat the seed in a way similar to vertical drift, namely, to assume that seed perturbations (e.g., by gravity waves) are omnipresent and that the lack of seed perturbations also is not the major cause of ESF variability patterns. Gravity waves may be the determining factor in the size of the ESF plumes, or in spatial periodicities of their appearance patterns [*Kelley et al.*, 1986], but not in whether or not ESF activity occurs on a given night.

Within the the framework described above, the occurrence of ESF becomes the expectation of each night within the "ESF season" at a given longitude. This is, after all, the basis of observed statistical studies and the planning basis for ESF observing campaigns. The lack of irregularity development thus becomes the exception to the rule.

We suggest that the absence of plume onset on a given night is due to the supression of instability growth rates by a transequatorial neutral wind. This ties the unusual case of no ESF to the equally unusual case of a strong meridional wind (as seen by *Sipler et al.* [1983]). We understand that the absence of a postsunset rise of the *F* region, or of gravity wave activity, might also be described as unusual. Indeed, ESF activity would be inhibited on such nights. Yet

observations presented here, as well as elsewhere, suggest that nights of no ESF activity can occur with a rising F region, with or without obvious seed perturbations. This again prompts us to associate periods of no ESF development with factors that inhibit an otherwise susceptible ionosphere to instability growth.

The concept and interpretation suggested here lends itself to testing by both experimental and computer simulation methods. Observationally, there are several longitude sectors where observations can be made at points along a flux tube that link the equatorial zone to the Appleton anomaly/intertropical arc regions. Fabry-Perot measurements of neutral winds using 6300-Å emission near the anomaly regions can be compared to irregularity onset and development patterns observed near the magnetic equator. A distribution of longitudes could be used, ranging from the Ascension Island region in the eastern Atlantic, the Forteleza-Cachoeria Paulista sites in Brazil, the Jicamarca-Arequipa sites in Peru, to Kwajalein-Wake Island in the Western Pacific, and a chain of sites in India. Archived data sets exists from some of these sites (*Sipler et al.* [1983] at Kwajalein, and *Biondi et al.* [1988] at Arequipa) that should be reexamined for evidence of ESF-neutral wind associations.

In the area of computer modeling, simulation studies are underway [*Zalesak and Huba*, 1991]. We urge that modeling results be obtained for a comprehensive set of observable parameters ($N_e(h)$ profiles, TEC patterns, airglow morphology, plasma drift, and neutral winds) in order to constrain the input-output conditions for the still intriguing and elusive explanation of equatorial spread F.

Acknowledgments. ALTAIR backscatter data collected during the PEAK 1988 campaign was funded by the Defense Nuclear Agency under contract DNA001-87-C-0169 to SRI International. The optical and radio-beacon observations and analyses were supported at Boston University as part of the JOHANNA Campaign under contracts from NASA (NAS8-36324), AFGL (F19628-86-K-0026), NSF (ATM-8709487) and ONR (N00014-89-J-1754). We are grateful for the discussions with Steven Zalesak, Henry Rishbeth, David Anderson, and Jules Aarons on various aspects of this work. We appreciate the cooperation of John Lansinger of Northwest Research Associates in providing the Polar BEAR TEC observations and Richard Doe (Boston University) and John Klobuchar (AFGL) for the Wake Island TEC data.

The editor thanks D. Sipler and another referee for their assistance in evaluating this paper.

REFERENCES

Aarons, J., The role of the ring current in generating F-layer irregularities during magnetic storms, Part 2, Equatorial latitudes, *Radio Sci., 26*, 1131, 1991.

Anderson, D. A., Modeling ambient low-latitude F region ionosphere—A review, *J. Atmos. Terr. Phys., 43*, 753, 1981.

Anderson, D. N., J. M. Forbes, and M. Codrescu, A fully analytic, low- and middle-latitude ionospheric model, *J. Geophys. Res., 94*, 1520, 1989.

Barbier, D., G. Weill, and J. Glaume, L'emission de la raie ronge du ciel nocturne en Afrique, *Ann. Geophys., 17*, 305, 1961.

Baumgardner, J., and S. Karandanis, CCD imaging system uses video graphics controller, *Electron. Imaging 3*, 28, 1984.

Biondi, M. A., J. W. Meriwether, Jr., B. Fejer, and R. Woodman, Measurements of the dynamics and coupling of the equatorial thermosphere and the F region ionosphere over Peru, *J. Atmos. Terr. Phys., 50*, 937, 1988.

Bittencourt, J. A., and M. A. Abdu, A Theoretical comparison between apparent and real vertical ionization drift velocities in the equatorial F region, *J. Geophys. Res., 86*, 2451, 1981.

Chandra, S., E. I. Reed, B. E. Troy, Jr., and J. E. Blamont, Equatorial airglow and the ionospheric geomagnetic anomaly, *J. Geophys. Res., 78*, 4630, 1973.

Das Gupta, A., A. Maritra, and S. K. Das, Postmidnight equatorial scintillation activity in relation to geomagnetic disturbances, *J. Atmos. Terr. Phys., 47*, 911, 1985.

Fejer, B. G., E. R. de Paula, I. S. Batista, E. Bonelli, and R. F. Woodman, Equatorial F region vertical plasma drifts during solar maxima, *J. Geophys. Res., 94*, 12,049, 1989.

Fremouw, E. J., and J. M. Lansinger, Characteristics of one-way propagation observed with "Rover" during PEAK 88, Tech. Rep. *CR-89-R046*, Northwest Res. Assoc. Inc., Bellevue, Wash., 1989.

Gaydukov, V. Yu., N. M. Kashchenko, M. A. Nikitin, and Yu. A. Romanovskiy, The stimulation of equatorial plasma bubbles by H_2O injection, *Geomagn. and Aeron., 29*, 392, 1989.

Haerendel, G., J. V. Eccles, and S. Cakir, Theory for modeling the equatorial evening ionosphere and the origin of the shear in the horizontal plasma flow, *J. Geophys. Res., 97*, 1209, 1992.

Hanson, W. B., B. L. Cragin, and A. Dennis, The effect of vertical drift on the equatorial F region stability, *J. Atmos. Terr. Phys., 48*, 205, 1986.

Hedin, A. E., MSIS-86 thermospheric model, *J. Geophys. Res, 92*, 4649, 1987.

Kelley, M. C., *The Earth's Ionosphere: Plasma Physics and Electrodynamics, Int. Geophys. Ser.*, vol. 43, Academic, San Diego, Calif., 1989.

Kelley, M. C., M. F. Larsen, C. A. Lattoz, and J. P. McClure, Gravity wave initiation of equatorial spread F: A case study, *J. Geophys. Res., 86*, 9087, 1981.

Kelley, M. C., J. LaBelle, E. Kudeki, B. G. Fejer, S. Basu, Su. Basu, K. D. Baker, C. Hanuise, P. Argo, R. F. Woodman, W. E. Swartz, D. T. Farley, and J. W. Meriwether, Jr., The Condor equatorial spread F campaign: Overview and results of the large-scale measurements *J. Geophys. Res., 91*, 54, 87, 1986.

Koster, J. R., Equatorial scintillation, *J. Planet. Space Sci., 10*, 1999, 1972.

Maruyama, T., A diagnostic model for equatorial spread F, 1, Model description and application to electric field and neutral wind effects, *J. Geophys. Res., 93*, 14,611, 1988.

Maruyama, T., and N. Matuura, Longitudinal variability of annual changes in activity of equatorial spread F and plasma bubbles, *J. Geophys. Res., 89*, 10,903, 1984.

Mendillo, M., and J. Baumgardner, Airglow characteristics of equatorial plasma depletions, *J. Geophys. Res., 87*, 7641, 1982.

Mendillo, M., H. Spence, and S. Zalesak, Simulation studies of ionospheric airglow signatures of plasma depletions at the equator, *J. Atmos. Terr. Phys., 47*, 885, 1985.

Meriwether, J. W., M. A. Biondi and D. N. Anderson, Equatorial airglow depletions induced by thermospheric winds, *Geophys. Res. Lett., 12*, 487, 1985.

Ossakow, S. L., Spread F theories—A review, *J. Atmos. Terr. Phys., 43*, 437, 1981.

Ossakow, S. L., S. T. Zalesak, B. E. McDonald, and P. K. Chaturvedi, Nonlinear equatorial spread F dependence on altitude of the F peak and bottomside background electron density gradient scale length, *J. Geophys. Res., 84*, 17, 1979.

Sipler, D. P., M. A. Biondi, and R. G. Roble, F region neutral winds and temperatures at equatorial latitudes: Measured and predicted behavior during geomagnetically quiet conditions, *Planet. Space Sci, 31*, 53, 1983.

Trost, T. F., Electron concentrations in the E and upper D region at Arecibo, *J. Geophys. Res., 81*, 2736, 1979.

Tsunoda, R. T., Time evolution and dynamics of equatorial backscatter plumes, 1, Growth phase, *J. Geophys. Res., 86*, 139, 1981.

Tsunoda, R. T., On the generation and growth of equatorial backscatter plumes, 2, Structuring of the west walls of upwellings, *J. Geophys. Res., 88*, 4869, 1983

Tsunoda, R. T., Control of the seasonal and longitudinal occurrence of equatorial scintillations by the longitudinal gradient in integrated E region Pedersen conductivity, *J. Geophys. Res., 90*, 447, 1985.

Tsunoda, R. T., and B. R. White, On the generation and growth of equatorial backscatter plumes, 1, Wave structure in the bottomside *F* layer, *J. Geophys. Res., 86*, 3610, 1981.

Tsunoda, R. T., M. J. Baron, J. Owen, and D. M. Towel, ALTAIR: An incoherent scatter radar for equatorial spread *F*, *Radio Sci., 14*, 1111, 1979.

Weber, E. J., J. Buchau, R. H. Eather, and S. B. Mende, North-south aligned equatorial airglow depletions, *J. Geophys. Res., 83*, 712, 1978.

Zalesak, S. T. and J. D. Huba, Effect of meridional winds on the development of equatorial spread *F*, *Eos Trans. AGU*, supplement, 211, April 23, 1991.

Zalesak, S. T. and S. L. Ossakow, On the prospect for artificially inducing equatorial spread *F*, *Mem. Rep.* 4899, Nav. Res. Lab., Washington, D.C., Sept. 1982.

Zalesak, S. T., S. L. Ossakow, and P. K. Chaturvedi, Nonlinear equatorial spread *F*: The effect of neutral winds and background Pedersen conductivity, *J. Geophys. Res., 87*, 151, 1982.

J. Baumgardner, M. Mendillo, X. Pi, and P. J. Sultan, Center for Space Physics, Boston University, Boston, MA 02215.

R. Tsunoda, SRI International, Menlo Park, CA 94025.

(Received August 22, 1991;
revised March 3, 1992;
accepted March 4, 1992.)